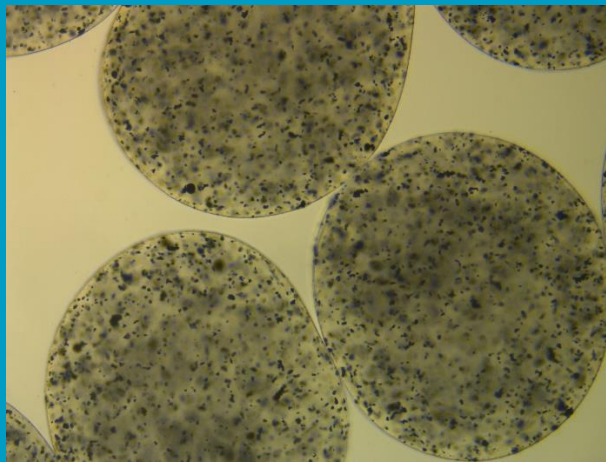# THE PRODUCTION AND CHARACTERISATION OF MAGNETIC PARTICLES PRODUCED WITH IN-AIR MICROFLUIDICS

Niek Monchen

Faculty of Engineering Technology
Program of Mechanical Engineering
Chair of Engineering Fluid Dynamics

UNIVERSITY OF TWENTE.

The production and characterisation of magnetic particles created with in-air microfluidics

N. Monchen

University of Twente, Faculty of Engineering Technology, Drienerlolaan 5, 7522 NB, Enschede, The Netherlands

ABSTRACT: Magnetic particles are widely used in biomedical, environmental and research applications. However, conventional production methods lack flexibility and are relatively expensive. Here we use in-air microfluidics to produce particles using a two-nozzle setup. The focus of this work is on magnetic particles that consist of a polymer matrix that is seeded with magnetic microparticles. Via in-air microfluidics monodisperse magnetic alginate particles are produced with neodymium and permalloy powder in mass percentages of 0.5%, 5% and 10%. The particles are then characterised in a custom-made setup by measuring the trajectories in water under influence of a magnetic field and comparing these to theory, revealing a decent resemblance. This research serves as a stepping stone for researchers who want to create their own magnetic particles with in-air microfluidics.

Key words: in-air microfluidics, magnetic particles, magnetic steering

1 INTRODUCTION

Encapsulated magnetic particles are increasingly used in biomedical applications for drug delivery [1], immunoassay [2, 3], protein binding and separation [4], magnetic hyperthermia [5], MRI scans as contrast agent [6] and growing bacteria cultures [7]. Further biomedical applications are reviewed in [8, 9]. In addition, magnetic particles are used to remove heavy metals from wastewater [10, 11, 12] and in fundamental research [13, 14].

The focus of this work is on magnetic particles that consist of a polymer matrix that is seeded with magnetic microparticles. A magnetic field can move or vibrate magnetic particles, for example, such that particles can be actuated remotely through other media. Together with the geometry of the particle and the dispersion of the magnetic particles inside it, particles have been tailored to specific sizes of $150\,\text{nm} - 330\,\text{nm}$ using coprecipitation [11] to $2.5\,\text{mm}$ using syringe dripping [10].

1.1 Production techniques

The fabrication of magnetic particles was pursued via various methods as summarized in Table 1. Traditionally, co-precipitation is used [15, 16, 17, 11]. Here, precipitation of a soluble substance is induced during stirring. A major drawback of this method is the time it takes for the liquid to evaporate and form particles, which can be tens of hours. Besides, chemical knowledge of the reactions is required. Chip microfluidics is faster for small batches [1, 7], yet developing and operating the required chips is challenging.

In-air microfluidics is a recently developed state-of-the-art production method. Monodisperse droplets are created by breaking up a jet to then crosslink these. This method is extremely fast as compared to chip microfluidics and almost as-controlled, while the components needed are easily obtainable. The size of the particles can be dictated by switching the nozzle size, thus enabling a flexible setup.

It has already been proven that magnetic particles can be created with in-air microfluidics, yet this is only limited to magnetic Janus particles for steerable micro-reactors [18]. Janus particles that have a magnetic and a non magnetic side allow the use for specific applications, like the rotation of particles by applying a sinusoidal magnetic field [19]. Janus particles were produced with up to twenty compartments using a twenty channel microfluidic chip [20]. In this research the focus will be on isotropic particles.

1.2 Research goal

The goal of this research is to fabricate magnetic particles via in-air microfluidics and assess their

magnetic properties in detail. In order to make these particles more appealing for research applications materials will be selected to maximise the magnetic response. The following questions will be answered:

- Is in-air microfluidics an appropriate method to produce monodisperse magnetic particles?

- How is the trajectory of such magnetic particles immersed in a fluid predicted when being subjected to a magnetic field?

2 THEORY

The motion of magnetic particles subjected to a magnetic field is one of the main interests, for which equations of motion based on Newton's second law are employed [8, 22, 23, 7]. A magnetic particle immersed in a fluid has the following equation of motion: Equation 1 where F_M is the magnetic force, F_D is the drag force and F_B is the buoyancy force. As we assume that the particles are suspended, the friction force is disregarded.

$$\sum \vec{F} = m\vec{a} = \vec{F}_M + \vec{F}_D + \vec{F}_B \tag{1}$$

The force on a magnetic particle in a vacuum is shown in Equation 2. For a derivation, see [24].

$$\vec{F}_M = \frac{V_{pow}\chi_V}{\mu_0}\vec{B}\nabla\vec{B} \tag{2}$$

Here V_{pow} [m³] is the volume of the magnetic powder within the particle, μ_0 [H m⁻¹] the permeability of free space, $\vec{B}$ [T] the magnetic flux density and $\nabla\vec{B}$ [T m⁻¹] is its gradient over $\vec{x}$ [m], which is defined as the position. The magnetic force is dependent on the volume susceptibility of the material, χ_V [-], which is usually determined experimentally as will be elaborated in subsection 3.3.

An important assumption for Equation 2 is that the magnetic dipoles of the powder do not influence each other and work in the same direction. Besides, the susceptibility of the polymer matrix and the surrounding of the particle should be much less than the susceptibility of the magnetic material. Care should be taken to use units consistently, as there are more than eight units for the magnetic field and magnetic flux.

Equation 2 is a practical version often used by scientists [24], using B [T] instead of H [A m⁻¹], the applied magnetic field. This follows from Equation 3, which depicts the relation of the flux density and applied magnetic field. In a vacuum, $\mu_r = 1$. The relation of the volume susceptibility χ_V with μ_r is described in Equation 4. μ_r can be acquired from a VSM measurement, later to be conducted.

$$B = \mu H \rightarrow B = \mu_r\mu_0 H \tag{3}$$

$$\chi_V = \mu_r - 1 \rightarrow \chi_V = \frac{1}{\mu_0}\frac{dB}{dH} - 1 \tag{4}$$

Equation 2 can be rewritten to a form in which the applied magnetic field is used instead of the magnetic flux density, shown in Equation 5. Here χ_V is used instead of μ_r. In this study this equation is used.

$$\vec{F}_m = \mu_0 V_{pow}\chi_V \vec{H}\nabla\vec{H} \tag{5}$$

The drag force is shown in Equation 6. Here, C_D [-] is the drag coefficient as defined in Equation 7 [25] with α [-] as calibration coefficient, A [m²] the frontal area of the particle and $\vec{v}$ [m s⁻¹] the velocity of the particle.

$$\vec{F}_D = -\frac{1}{2}\rho_f C_D A\vec{v}|\vec{v}| \tag{6}$$

$$C_D = \alpha\left(\frac{24}{Re}\left(1 + 0.150Re^{0.681}\right) + \frac{0.407}{1 + \frac{8710}{Re}}\right) \tag{7}$$

For the drag force often Stokes law is used, which is defined as $C_D = \frac{24}{Re}$ with $Re \equiv \rho_f|\vec{v}|D/\mu$. With ρ_f [kg m⁻³] the density of the fluid, D [m] the diameter of the particle, μ [Pa s] the dynamic viscosity of the fluid and R [m] the radius of the particle, substituting this results in Equation 8. Stokes law is only valid for $Re < 1$ and in our

Table 1: Characteristics of the production of magnetic particles for several papers.

Paper	Production method	Magnetic Material	Copolymer	Diameter	Magnetic component %	Time Per batch	Application
[10]	syringe dripping	superparamagnetic maghetite (ferrofluid)	alginate	2.5 mm mean	1:10 ratio	30+ m	heavy metal removal
[11]	coprecipitation	magnetite	ethylene glycol	150 nm – 330 nm	×	10+ h	heavy metal removal
[16]	coprecipitation	magnetite	PS-AA PS-AA PS-BA	4.6 µm – 39.4 µm	25% (wt./wt.)	340+ m	×
[15]	coprecipitation	magnetite	nitrocellulose	125 µm – 250 µm	×	34+ h	magnetically fluidized bed or magnetic filtration
[17]	coprecipitation	maghemite chromium dioxide oleic acid-coated magnetite	EDMA GMA	1.5 µm – 2.05 µm	9.2-12.4% (wt./wt.)	23.5+ h	×
[18]	in-air microfluidics	amino superparamagnetic microparticles	alginate	7 µm – 15 µm	1-9% (v./v.)	4 m	×
[21]	Dripping	magnetite	alginate	×	×	13.5+ h	heavy metal removal
[7]	microfluidic chip	magnetite	alginate	800 µm – 1100 µm	×	×	bacteria culturing and magnetic separation
[1]	microfluidic chip	magnetite	chitosan	40 µm – 200 µm	×	×	smart drug delivery

4

system, this condition is violated, thus it is chosen to use Equation 6.

$$\vec{F}_D = -3\pi\mu D\vec{v} \tag{8}$$

In literature it has already been shown that the boundary layer of a hydrogel does not behave like a smooth sphere. For hydrogel particles with low and high Re significant drag reduction has been found [26, 27]. Therefore it it chosen to calibrate the drag coefficient using experiments where falling particles were tracked in absence of a magnetic field. This is done with the coefficient α.

At last, the buoyancy force is added:

$$\vec{F}_B = -V_{par}(\rho_{par} - \rho_f)\vec{g} \tag{9}$$

Here V_{par} [m³] and ρ_{par} [kg m⁻³] are the volume and density of the particle respectively and $\vec{g}$ [m s⁻²] is the gravitational acceleration.

For an incompressible fluid with zero viscosity the added added mass effect is incorporated by adding half of the moved fluid to the total mass, m [kg], that needs to be accelerated [28].

$$m = m_{par} + \frac{1}{2}V_{par}\rho_f \tag{10}$$

Rewriting m_{par} [kg] as a function of the volume and powder mass percentage such that it can be calculated during the characterisation.

$$m = \frac{V_{par}}{\frac{1-x_{pow}}{\rho_h} + \frac{x_{pow}}{\rho_{pow}}} + \frac{1}{2}V_{par}\rho_f \tag{11}$$

with x_{pow} [-] the mass powder percentage in the particle, ρ_h [kg m⁻³] the density of the alginate and ρ_{pow} [kg m⁻³] the density of the powder.

This gives us the second order nonlinear differential Equation 12. This equation of motion is solved numerically using the Runge-Kutta method.

3 METHODS

3.1 In-air microfluidics

The main principle of in-air microfluidics is the exploitation of Rayleigh Plateau instability, which dictates the capillary breakup of a jet into droplets. Rayleigh derived a dispersion relation which is valid in the non-viscous limit, which shows that the fastest growing pertubation is reached if kR_0 = 0.697 [29], with R_0 being the nozzle radius. A simplified version is shown in Equation 13, with ω [rad s⁻¹] as the frequency, σ [N m⁻¹] as the surface tension and ρ [kg m⁻³] as the fluid density. In-air microfluidics exploits this by artificially activating this mode using a vibrating element, such as a speaker of piezo, such that the jet breaks up at a constant rate creating monodisperse droplets. In practice however, parasitic eigenfrequencies of the setup or eigenfrequencies of the vibrating element can influence the optimum frequency.

$$\omega^2 \approx \frac{\sigma}{\rho R_0^3}0.1332 \tag{13}$$

Once a steady flow of monodisperse droplets is created, the droplets need to be solidified. This is done by crosslinking, e.g. using an intercepting crosslinking fluid or using photoinitiation by UV light, depending on the chemical formulation.

In this study we use a main jet of 0.5% sodium alginate 80-120, which is intercepted by a side-jet of 0.5 mol L⁻¹ calciumchloride and 10% ethanol. Figure 3 A shows an overview of this process. The blue jet displays the alginate jet with powder, breaking up in monodisperse droplets. After this occurs, the calciumchloride is used to crosslink the alginate, while the ethanol is added to lower the surface tension. Its purpose is to enhance the marangoni effect, which is driven by a gradient in surface tension, encapsulating the droplet while the calciumchloride diffuses to its center. Subsequently, the particles are collected

$$\frac{d^2\vec{x}}{dt^2} = \frac{\mu_0 V_{pow}\chi_V \vec{H}\nabla\vec{H} - \frac{1}{2}\rho_f C_D A\frac{d\vec{x}}{dt}|\frac{d\vec{x}}{dt}| - V_{par}(\rho_{par} - \rho_f)\vec{g}}{\frac{V_{par}}{\frac{(1-x_{pow})}{\rho_h} + \frac{x_{pow}}{\rho_{pow}}} + \frac{1}{2}V_{par}\rho_f} \tag{12}$$
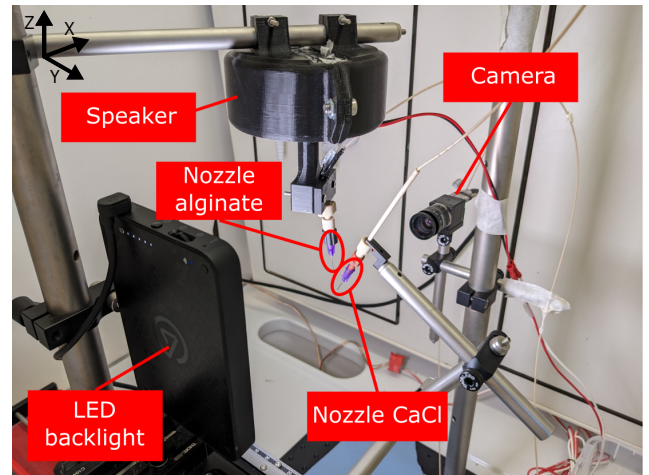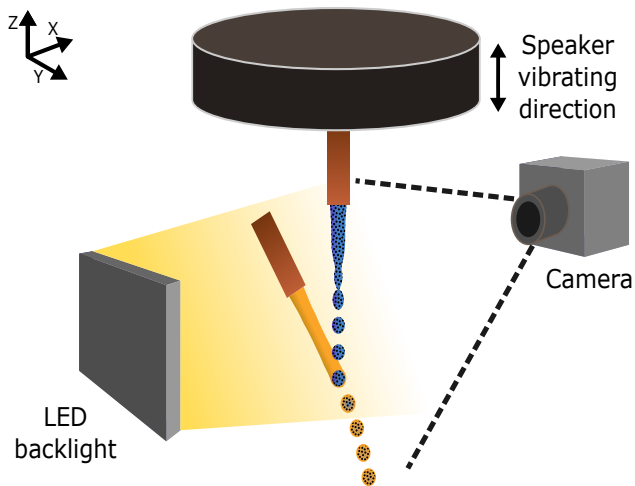
Fig. 1: The setup which was used to perform the experiments to create magnetic particles.

in a petri dish with a layer of the calciumchloride solution.

The setup which was used can be seen in Figure 1. The alginate nozzle is vibrated by a woofer, which works at low frequencies. The calciumchloride nozzle can be moved by a 3D stage. To view and record the process, a XIMEA MC031MG-SY camera with a LED backlight is used.

Particles with a starting powder alginate wt./wt. ratio of 0.5%, 5% and 10% were produced using a 0.52 mm ID nozzle. Later extra larger particles were produced using a nozzle of 0.84 mm with 10% wt./wt. ratio. Note that the percentages are before producing the particles and may differ afterwards.

3.2 Powder characterisation

The goal of the particles is to maximize the magnetic force without increasing the magnetic field as this is often a constraint. Using Equation 5, the material dependent properties can be found. As the volume of powder inside a particle is limited, the only material dependent property left influencing the magnetic force is the magnetic susceptibility χ_V.

Two powders have been employed in this sudy: neodymium powder (25 µm) and permalloy (45 µm max, Sigma Aldrich). Neodymium is known as a strong permanent magnetic material and not for its high susceptibility. Permalloy is an alloy of 81% nickel and 19% iron, known for its high susceptibility. This was readily available and due to time constraints permalloy was chosen.

To determine the morphology of the powders, both were analysed with the JCM-5000 Neo-Scope™ Table Top SEM. Pure powders were put onto a disk with double-sided tape and loaded into the SEM. The images taken with the SEM of the powders are shown in Figure 2. Both these images were taken at 5 kV and 220 times magnification. A distinct difference can be seen between neodymium and permalloy. Where neodymium has a more granular structure, permalloy consists of relatively spherical particles. Generally, neodymium particles do not differ significantly in size while the diameter ratio between the largest and smallest particles is at least ten times for permalloy. Considerable agglomeration of particles can be seen for neodymium, while this is more difficult to observe for permalloy.

To measure the magnetic properties of the powder, the PPMS® DynaCool™ Vibrating Sample Magnetometer (VSM) was used from Quantum Design. The powder was loaded into a gelatine capsule and then fixed with glue. The capsule was inserted in the tube and held in place by a string. The measurements for the neodymium were done from 0.5 T to –0.5 T to 0.5 T with a step size of 0.01 T. For permalloy these were from 1 T to –1 T to 1 T with a step size of 0.01 T.

With the VSM measurements the hysteresis loops could be determined, shown in Figure 2.
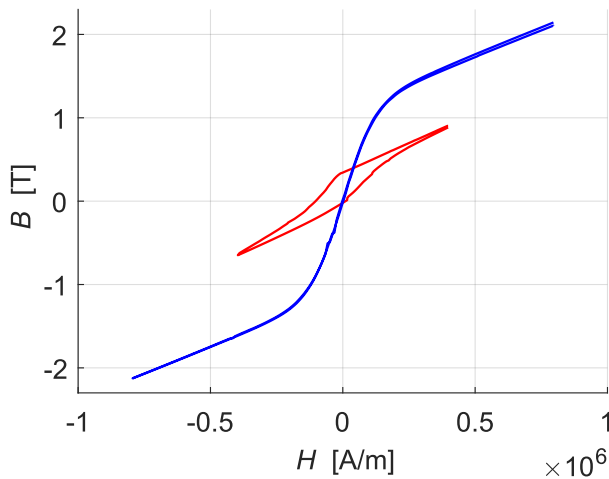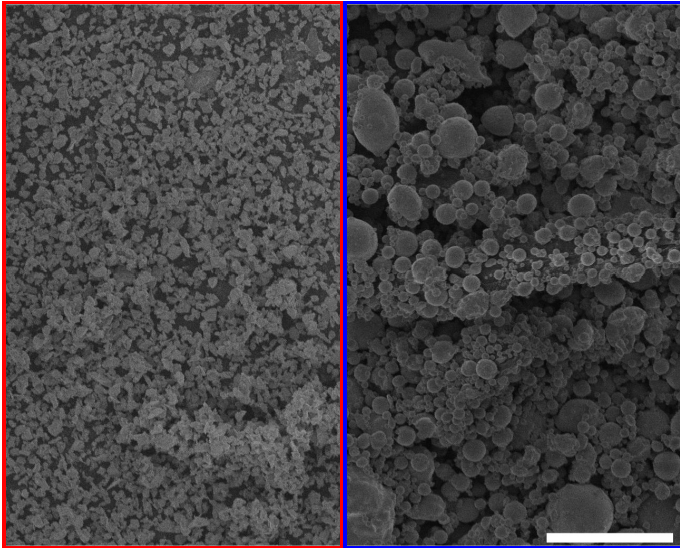
Fig. 2: (Top) Pictures made with the SEM of both neodymium powder (red) and permalloy powder (blue). The scale bar is 100 μm. Both images were taken at 5 kV and 220 times magnification. (Bottom) Hysteresis loops of neodymium (red) and permalloy (blue) measured with the VSM.

Due powder structure of the material, the complete fixation of the particles is a challenging task, resulting in some errors in the measurements. This can be observed in the bumps appearing in the line, which indicate shifting of the powder.

Nevertheless, the typical behaviour of a strong permanent magnetic material like neodymium is clearly visible with a high retentivity without any magnetic field applied. In the case of permalloy the hysteresis is hardly present. This was to be expected as permalloy does not have a strong retentivity.

The relative permeability μ_r as function of the ap-

plied magnetic field H is obtained from the slope of the hysteresis loops. The steeper the slope the higher the susceptibility of the material, thus the stronger it reacts to a magnetic field. Although the measurement of the neodymium only reaches half of the applied magnetic field as that of permalloy, the susceptibility of permalloy is significantly higher close to zero. As the magnetic field can be a limiting factor, the susceptibility at a lower magnetic field strength is the most essential.

3.3 Particle characterisation

The particles were laid on a backlight and photographed using a Nikon D610 Camera and a macro lens with 60 mm focal length. Only for alginate particles without powder the LED backlight was removed. The images were then postprocessed by converting it to grayscale and consequently the images of particles with powder were binarised and for those without powder CLAHE was applied. The particles were detected with a Hough Transform using MATLAB and Python. The size distributions were fitted with a Gaussian.

Once the particles were produced, the 5% and 10% permalloy particles were tested[1], by measuring their reaction to a magnetic field using an electromagnet of which the magnetic field was measured over a straight line perpendicular to the magnet. An acryl container was placed in front of the electromagnet with a 2 mm wide pillar inside it. The particles were placed on this pillar and subsequently the magnet was turned on. A camera captured this process to be able to determine the trajectory. Figure 4 shows a schematic of the process.

The measured trajectory is compared with the theoretical trajectory based on the equation of motion of the magnetic particle Equation 12. The magnetic measurements described in subsection 3.2 were used for the susceptibility. The assumed powder content was taken slightly lower than the input weight as it turned out that a portion of the powder sank to the bottom of the syringe. Ultimately, the equations were solved using the Runge-Kutta method with the MATLAB

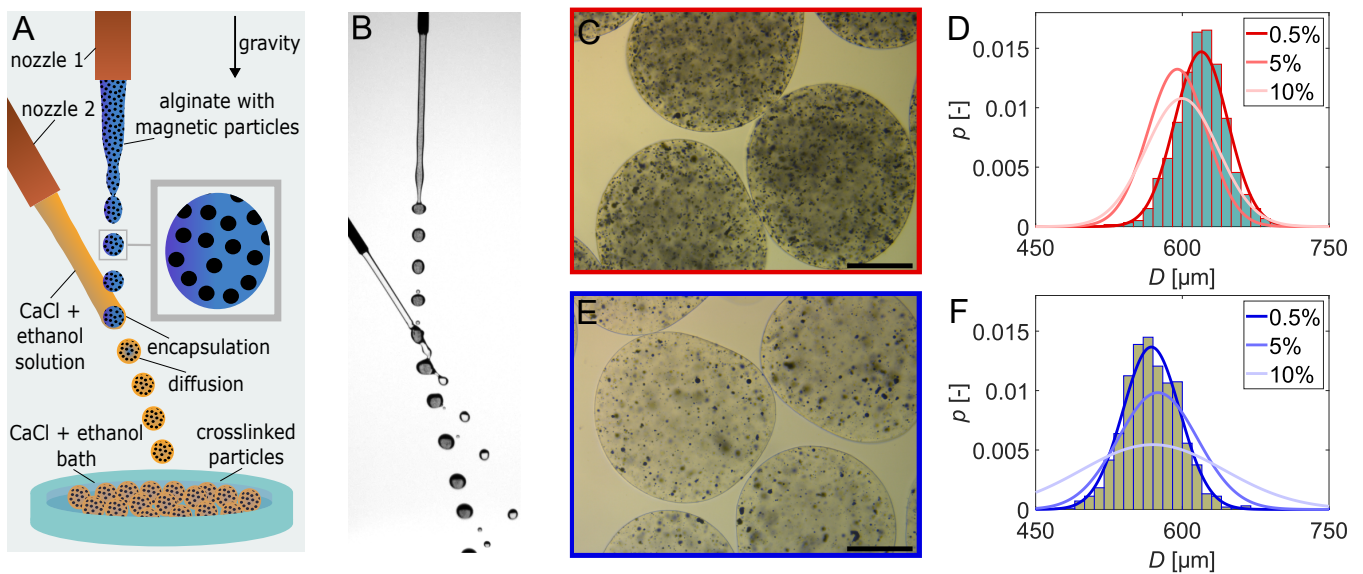[1] The magnet was not strong enough to attract the other particles.

Fig. 3: (A) Illustration of the process. Colours are for illustrative purposes only. (B) Photo of the process. (C) Alginate particles with 0.5% wt/wt permalloy powder. Scale bar is 250 µm. (E) Alginate particles with 0.5% wt/wt neodymium powder. Scale bar is 250 µm. (D & F) Gaussian fit of size distribution for neodymium (red) and permalloy (blue) with the histogram of the 0.5% samples.

command ode45.

4 RESULTS & DISCUSSION

4.1 Particle properties

Figure 3 B shows the process and Figure 3 C-F show the results of the production of the magnetic particles. Pictures taken under a Leica DM 300 microscope show homogeneous distribution of the powder inside the alginate particles, with the exception of occasional agglomeration of multiple particles or bigger particles. It should be noted that this is 2D and assuming a spherical shape, the middle of the particle should show the most powder or be the darkest, while the edges should be the lightest. Neodymium particles are significantly darker than permalloy particles.

Neodymium particles show size distributions which coincide relatively well, while the permalloy particles show a larger standard deviation with an increasing powder percentage. The powder percentage here indicates the wt./wt. percentage before production. For both powders an increase in powder percentage is accompanied with an increase in standard deviation in the size distribution. The particles look spherical, al-

though for higher powder percentages the particles show more abnormalities.

4.2 Characterisation

The theoretical trajectories are compared with the experimental measurements in Figure 4 B and C. Here, for visual purposes, the x and y coordinates are normalised by their starting and ending coordinate respectively. In Figure 4 D and E normalised x has been plotted against time, showing the most dominant movement direction. Generally, the theoretical fit follows the experimental measurement closely. The largest errors occur at the end of the trajectories, where the speed is the highest. The actual errors between the experiments and theory are in the order of magnitude of the diameter of the particle.

A scaling has been applied in Figure 4 F. Here, the scaling implies a case of a constant magnetic field in time where the magnetic force is dominant, which is the case for most of the trajectory. The added mass effect has been incorporated as well.
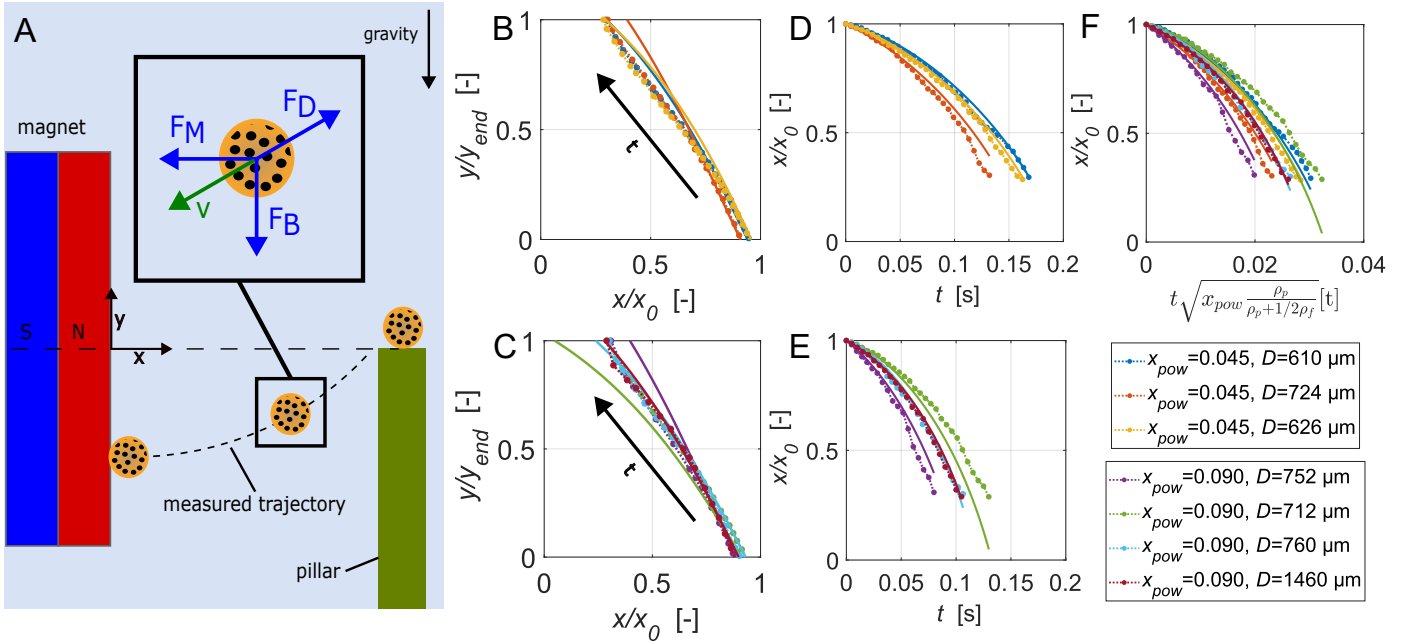
8

Fig. 4: (A) Schematic of the process in the characterisation setup. (B) $x - y$ plot of the trajectories for $x_{pow} = 0.05$. (C) $t - x$ plot of the trajectories for $x_{pow} = 0.05$. (D) $x - y$ plot of the trajectories for $x_{pow} = 0.1$. (E) $t - x$ plot of the trajectories for $x_{pow} = 0.1$. (F) All trajectories with a scaling applied to the time.

4.3 Discussion

The addition of powder to the jet causes an increase in viscosity and affects the surface tension. The quantisation of these properties is difficult due to the non-perfect dispersion of powder in the jet, uneven sized powder and phenomena like wetting and agglomeration. The validity of the inviscid Equation 13 decreases with an increasing powder percentage due to the increasing viscosity. Nevertheless, it was possible to create monodisperse particles with both powders, although an increase in powder percentage showed larger deviations. At higher percentages it was observed that the breakup of the jet was more unstable, due to the powder influencing the breakup. A possible cause could be that the woofer was not reaching low enough frequencies or it was simply not possible to induce a clean breakup.

Furthermore, the importance of the microscopic structure of the magnetic particles for producing particles with in-air microfluidics seems to be negligible. More crucial properties are the diameter and density, as this causes particles to sink quicker and stay on the bottom, thus resulting in less magnetic particles in the jet. As the two pow-

ders have different size distributions and densities this would explain the diverging results as seen in Figure 3 C and E. Dispersing the powder in the syringe was a difficult task. A partial solution could be to sieve the powder which would improve the consistency by removing particles which quickly sink to the bottom. The dispersion of particles in the syringe and jet is a problem which needs to be looked into, either by implementing a solution with the syringe pumps or replacing the entire pumping system.

Even though the drag of the particles has been roughly calibrated and the magnetic field was only measured in one line perpendicular to the magnet, the theory corresponds well to the experiments. There is some deviation at the end of the trajectories, which can partly be accounted to the trajectories diverting from the line on which the magnetic field is measured, shown in Figure 4 A. Therefore it is recommended to measure the entire field with a 3D-probe for future research.

The scaling shows that the trajectories, having slightly different initial values, can be related to each other when the magnetic field is constant in time and the magnetic force is dominant. Using this scaling it can be approximated how much

powder is in a particle, by measuring its trajectory.

The setup was limited in capabilities as only two types of particles could be tested. The magnetic field created by the magnet was the bottleneck and therefore a stronger magnet would increase the capabilities of the setup. A longer trajectory would help to increase the precision of the measurements. The testing of a wider range of particle sizes and powder percentages would increase the certainty greatly.

5 CONCLUSIONS

In-air microfluidics has shown to be a useful method for creating monodisperse magnetic particles. Although it must be noted there is a trade-off between monodispersity and the susceptibility when creating particles, it has been proven that the creation of magnetic particles with this method is has been successful. The characterisation showed that the behaviour of the particles is well described. This research serves as a stepping stone for researcher who want to produce their own magnetic particles using in-air microfluidics.

For future research it is recommended to further investigate the breakup mechanisms when powder is included. In addition, increasing the magnet strength of the characterisation setup will enhance the precision. Moreover, the production of magnetic particles with in-air microfluidics creates opportunities for the creation of non-spherical particles, like magnetic fibers.

REFERENCES

1. X. Gong, S. Peng, W. Wen, P. Sheng, and W. Li, "Design and fabrication of magnetically functionalized core/shell microspheres for smart drug delivery," *Advanced Functional Materials*, vol. 19, no. 2, pp. 292–297, jan 2009. doi:10.1002/ADFM.200801315.

2. J. L. Guesdon, R. Thierry, and S. Avraméas, "Magnetic enzyme immunoassay for measuring human IgE," *The Journal of Allergy and Clinical Immunology*, vol. 61, no. 1, pp. 23–27, 1978. doi:10.1016/0091-6749(78)90469-4.

3. K. W. Bong, S. C. Chapin, and P. S. Doyle, "Magnetic barcoded hydrogel microparticles for multiplexed detection," *Langmuir*, vol. 26, no. 11, pp. 8008–8014, jun 2010. doi:10.1021/la904903g.

4. T. Banert and U. A. Peuker, "Synthesis of Magnetic Beads for Bio-Separation Using the Solution Method," *Chemical Engineering Communications*, vol. 194, no. 6, pp. 707–719, jun 2007. doi:10.1080/00986440600992750.

5. B. E. Kashevsky, S. B. Kashevsky, V. S. Korenkov, Y. P. Istomin, T. I. Terpinskaya, and V. S. Ulashchik, "Magnetic hyperthermia with hard-magnetic nanoparticles," *Journal of Magnetism and Magnetic Materials*, vol. 380, pp. 335–340, apr 2015. doi:10.1016/J.JMMM.2014.10.109.

6. H. Shokrollahi, A. Khorramdin, and G. Isapour, "Magnetic resonance imaging by using nano-magnetic particles," *Journal of Magnetism and Magnetic Materials*, vol. 369, pp. 176–183, nov 2014. doi:10.1016/J.JMMM.2014.06.023.

7. S. Yuan, P. T. Lai, A. H. Shum, and P. W. Pong, "Magnetic-Particle-Encapsulated Alginate Beads for Aqueous-Based Bacteria Culturing and Manipulation," *IEEE Transactions on Magnetics*, vol. 58, no. 2, feb 2022. doi:10.1109/TMAG.2021.3102959.

8. M. A. Gijs, "Magnetic bead handling on-chip: new opportunities for analytical applications," *Microfluidics and Nanofluidics 2004 1:1*, vol. 1, no. 1, pp. 22–40, oct 2004. doi:10.1007/S10404-004-0010-Y.

9. M. Shinkai and A. Ito, "Functional magnetic particles for medical application." *Advances in biochemical engineering/biotechnology*, vol. 91, pp. 191–220, 2004. doi:10.1007/B94212.

10. A. Idris, N. S. M. Ismail, N. Hassan, E. Misran, and A. F. Ngomsik, "Synthesis of magnetic alginate beads based on maghemite nanoparticles for Pb(II) removal in aqueous solution," *Journal of Industrial and Engineering Chemistry*, vol. 18, no. 5, pp. 1582–1589, sep 2012. doi:10.1016/J.JIEC.2012.02.018.

11. X. X. Zhou, Y. J. Li, and J. F. Liu, "Highly Efficient Removal of Silver-Containing Nanoparticles in Waters by Aged Iron Oxide Magnetic Particles," *ACS Sustainable Chemistry and Engineering*, vol. 5, no. 6, pp. 5468–5476, jun 2017. doi:10.1021/acssuschemeng.7b00797.

12. S. Moosavi, C. W. Lai, S. Gan, G. Zamiri, O. Akbarzadeh Pivehzhani, and M. R. Johan, "Application of efficient magnetic particles and activated carbon for dye removal from wastewater," *ACS Omega*, vol. 5, no. 33, pp. 20684–20697, aug 2020. doi:10.1021/acsomega.0c01905.

13. E. Falcon, J. C. Bacri, and C. Laroche, "Dissipated power within a turbulent flow forced homogeneously by magnetic particles," *Physical Review Fluids*, vol. 2, no. 10, p. 102601, oct 2017. doi:10.1103/PhysRevFluids.2.102601.

14. A. Cazaubiel, J. B. Gorce, J. C. Bacri, M. Berhanu, C. Laroche, and E. Falcon, "Three-dimensional turbulence generated homogeneously

by magnetic particles," *Physical Review Fluids*, vol. 6, no. 11, p. L112601, nov 2021. doi:10.1103/PhysRevFluids.6.L112601.

15. D. Tanyolaç and A. R. Özdural, "Preparation of low-cost magnetic nitrocellulose microbeads," *Reactive and Functional Polymers*, vol. 45, no. 3, pp. 235–242, oct 2000. doi:10.1016/S1381-5148(00)00037-7.

16. S. Omi, A. Kanetaka, Y. Shimamori, A. Supsakulchai, M. Nagai, and G. H. Ma, "Magnetite (Fe3O4) microcapsules prepared using a glass membrane and solvent removal," *Journal of microencapsulation*, vol. 18, no. 6, pp. 749–765, 2001. doi:10.1080/02652040110055252.

17. D. Horák, F. Lednický, E. Petrovský, and A. Kapička, "Magnetic Characteristics of Ferrimagnetic Microspheres Prepared by Dispersion Polymerization," *Macromolecular Materials and Engineering*, vol. 289, no. 4, pp. 341–348, apr 2004. doi:10.1002/MAME.200300271.

18. T. Kamperman, V. D. Trikalitis, M. Karperien, C. W. Visser, and J. Leijten, "Ultrahigh-Throughput Production of Monodisperse and Multifunctional Janus Microparticles Using in-Air Microfluidics," *ACS Applied Materials and Interfaces*, vol. 10, no. 28, pp. 23 433–23 438, jul 2018. doi:10.1021/ACSAMI.8B05227.

19. S. R. Wilson-Whitford, J. Gao, M. C. Roffin, W. E. Buckley, and J. F. Gilchrist, "Microrollers flow uphill as granular media," *Nature Communications*, vol. 14, no. 1, p. 5829, sep 2023. doi:10.1038/S41467-023-41327-1.

20. Z. Wu, Y. Zheng, L. Lin, S. Mao, Z. Li, and J. M. Lin, "Controllable Synthesis of Multicompartmental Particles Using 3D Microfluidics," *Angewandte Chemie International Edition*, vol. 59, no. 6, pp. 2225–2229, feb 2020. doi:10.1002/ANIE.201911252.

21. A. Bée, D. Talbot, S. Abramson, and V. Dupuis, "Magnetic alginate beads for Pb(II) ions removal from wastewater," *Journal of Colloid and Interface Science*, vol. 362, no. 2, pp. 486–492, oct 2011. doi:10.1016/j.jcis.2011.06.036.

22. K. Zhang, Q. Liang, S. Ma, X. Mu, P. Hu, Y. Wang, and G. Luo, "On-chip manipulation of continuous picoliter-volume superparamagnetic droplets using a magnetic force," *Lab on a Chip*, vol. 9, no. 20, pp. 2992–2999, oct 2009. doi:10.1039/B906229G.

23. Z. H. Wei, C. P. Lee, and M. F. Lai, "Magnetic particle separation using controllable magnetic force switches," *Journal of Magnetism and Magnetic Materials*, vol. 322, no. 1, pp. 19–24, jan 2010. doi:10.1016/J.JMMM.2009.08.029.

24. J. Svoboda, *Magnetic Techniques for the Treatment of Materials*, 1st ed. Dordrecht: Kluwer Academic Publishers, 2004. ISBN 1402021070. [Online]. Available: http://www.ebooks.kluweronline.com

25. P. P. Brown and D. F. Lawler, "Sphere Drag and Settling Velocity Revisited," *Journal of Environmental Engineering*, vol. 129, no. 3, pp. 222–231, mar 2003. doi:10.1061/(ASCE)0733-9372(2003)129:3(222).

26. A. M. Rashedul Kabir, D. Inoue, Y. Kishimoto, J.-I. Hotta, K. Sasaki, N. Kitamura, J. P. Gong, H. Mayama, and A. Kakugo, "Drag force on micron-sized objects with different surface morphologies in a flow with a small Reynolds number," *Polymer Journal*, vol. 47, pp. 564–570, 2015. doi:10.1038/pj.2015.29.

27. C. Tian, X. Wang, Y. Liu, W. Yang, H. Hu, X. Pei, and F. Zhou, "In Situ Grafting Hydrophilic Polymeric Layer for Stable Drag Reduction," *Langmuir*, vol. 35, no. 22, pp. 7205–7211, jun 2019. doi:10.1021/acs.langmuir.9b00321.

28. J. Pantaleone, . J. Messer, and J. Messer, "The added mass of a spherical projectile," *American Journal of Physics*, vol. 79, no. 12, pp. 1202–1210, dec 2011. doi:10.1119/1.3644334.

29. J. Eggers and E. Villermaux, "Physics of liquid jets," *Reports on Progress in Physics*, vol. 71, no. 3, p. 036601, feb 2008. doi:10.1088/0034-4885/71/3/036601.

Supplementary materials

CONTENTS

1   INTRODUCTION

In this document, additional material to the paper is supplied together with extensive explanation of the methods used.

2 MAGNETISM

To be able to understand the physics of magnetic particles, in this section the theory is studied and relevant mechanisms are identified.

2.1 Origin of magnetic field

First of all, it is of importance to understand where magnetism originates from. Each atom has a magnetic moment, which is the result of electrons moving around them. The orbital magnetic moment is a result of the electron spinning around the atom and the spin magnetic moment is a result of the electron spinning around its own axis. Together these form the total magnetic moment [1].

A magnetic field is often created by permanent magnets or electromagnets, which are used in numerous applications. Electromagnets are widely used in almost every electrical device, for relays, motors and transformers. Permanent magnets can be found in hard drives, credit cards, or simply as refrigerator magnet. Also, permanent magnets and electromagnets can be found in speakers where they work together to create sound waves.

All this is done by exploiting the properties of a magnetic field. A typical magnetic field can be seen in Figure 2.1. Every magnetic field, just like Earth's magnetic field, has a north and south pole where the magnetic field lines start and end respectively. Putting a compass (or piece of magnetic material) on the field lines would align the compass with the field line.
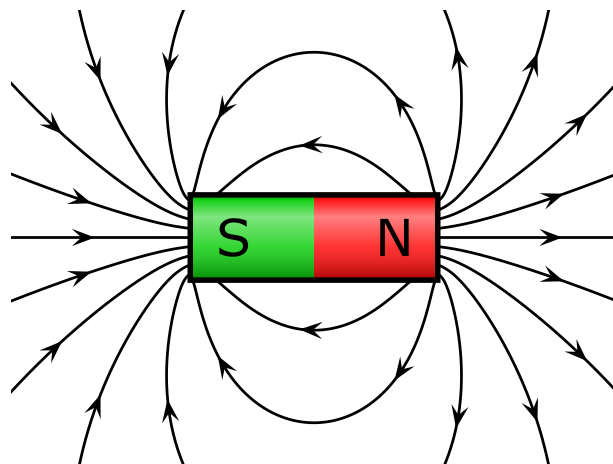
Figure 2.1: Magnetic field around a magnet. Retrieved from [2]. Licensed under CC BY-SA 3.0.

In the case of permanent magnets or magnetised materials, the magnetic field is caused by the magnetic moment in a material, which is essentially made up of the sum of the moments of each individual atom. The direction can change, resulting in a stronger response if more moments are pointed in the same direction and a weaker response when pointing in opposite direction [1].

For electromagnets the magnetic field is caused by the current going through the coil. The
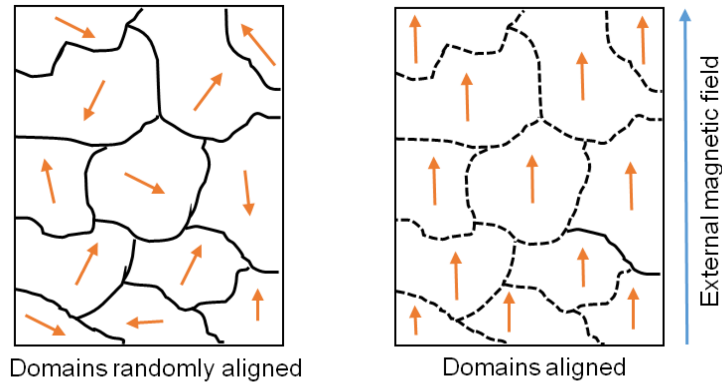
Figure 2.2: Schematic of magnetic domains in a material. This figure is reprinted/reused according to CC BY 4.0 [3].

magnetic field is dependent on the properties of this coil such as length, number of turns and wire thickness.

2.2 Magnetic flux density and applied magnetic field

As a consequence of the magnetic moment a magnetic field is formed around a magnetised object. The relation between the magnetic flux density $\vec{B}$ [T or $N\,A^{-1}\,m^{-1}$] and the applied magnetic field is shown in Equation 2.1 [4]. The applied magnetic field $\vec{H}$ [$A\,m^{-1}$] is multiplied by the susceptibility of the medium, which is μ [$N\,A^{-2}$]. For a vacuum $\mu = \mu_0$, also known as the permeability of free space.

$$\vec{B} = \mu\vec{H} \tag{2.1}$$

If an object in a magnetic field is magnetised, the relation Equation 2.2 is used. Here $\vec{M}$ [$A\,m^{-1}$] is the magnetisation of the material. The sum of $\vec{H}$ and $\vec{M}$ is then multiplied by μ_0 to get $\vec{B}$.

$$\vec{B} = \mu_0(\vec{H} + \vec{M}) \tag{2.2}$$

$\vec{M}$ can be related to $\vec{H}$ using the susceptibility χ, which is a material dependent property, shown in Equation 2.3 [4]. As explained in section 2.1 the magnetic field of a material is caused by the alignment of the magnetic moments in a material. The susceptibility basically is a measure for the degree of alignment of these moments and thus the magnetisation of the material.

$$\vec{M} = \chi\vec{H} \tag{2.3}$$

χ can also be described with the relative permeability μ_r, shown in Equation 2.4, as it might be more convenient in certain scenarios.

$$\mu_0(\vec{H} + \vec{M}) = \mu_0(1 + \chi)\vec{H} = \mu_r\mu_0\vec{H} = \mu\vec{H} \tag{2.4}$$

2.3 Hysteresis loop

Due to ability of materials to be magnetised and demagnetised, a characteristic loop is formed. This is called the hysteresis loop [4] and can be seen in Figure 2.3. When a material is completely demagnetised it will not have any influence on the flux density when a magnetising force is applied. When starting to apply a magnetising force, the material will start arranging its magnetic dipoles towards this direction, resulting in magnetisation of the material. This will continue

till the saturation point, where the flux density will not increase any more for an increasing magnetising force. When decreasing the magnetising force again, the material will now exhibit a stronger flux density. This is due to the fact that the material has been magnetised, which can be seen when the magnetising force reaches zero. It will then show retentivity, which results in a permanent magnet. Continuing towards a negative magnetising force, a point is reached which is called the coercivity of a material. This is the magnetising force needed to fully demagnetise a material. Strong permanent magnets like neodymium have a high retentivity and coercivity.
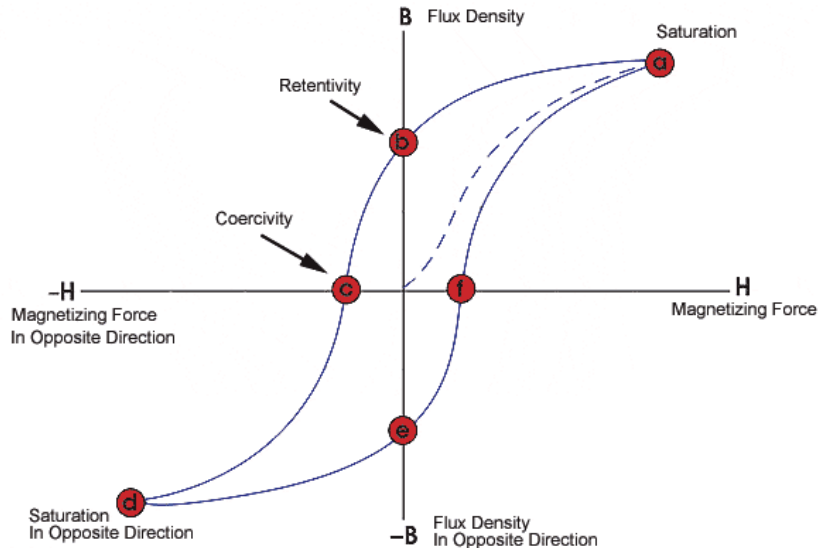
Figure 2.3: Hysteresis loop. This figure is reprinted/reused by permission from ©Iowa State University Center for Nondestructive Evaluation (CNDE)[5]. Licensed under CC BY-NC 4.0 International.

2.4   Types of magnetic materials

There are several types of magnetic behaviour a material can exhibit, namely ferromagnetism, paramagnetism, ferrimagnetism and antiferromagnetism. These are shown in Figure 2.4. Each type has its own typical relative permeability.

2.5   Curie temperature

The types of magnetic behaviour are directly related to the Curie temperature. The Curie temperature dictates the type of magnetic behaviour a material exhibits. When the temperature is below the Curie temperature a material will exhibit ferromagnetism and when above Curie temperature it will exhibit paramagnetism. Consequently, for the highest permeability the working temperature of these materials needs to be below Curie temperature. The Curie temperature typically ranges from about 310 °C to about 340 °C for neodymium magnets and is around 770 °C for iron [7].

2.6   Magnetic powder

Now that all relevant physics and mechanisms of magnetic materials have been discussed, this leads to the criteria for a magnetic powder. The requirement for for this material regarding magnetism would be to have a strong ferromagnetic response. A strong ferromagnetic response is characterised by the initial and/or relative permeability.
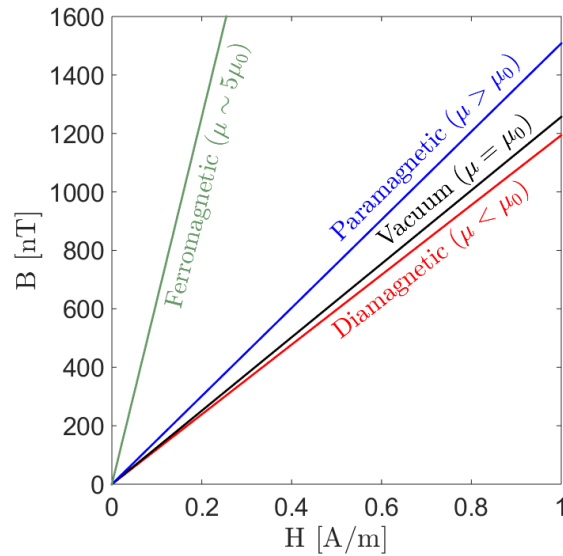
Figure 2.4: Visual indication of magnetic behaviour. This graphic is purely an indication of the order of magnitude and can differ per material. This figure is reprinted/reused according to CC BY 4.0 [6].

Besides a high permeability, the diameter of the largest particles in the powder should not be too large to clog the nozzle and it should be able to be dispersed properly into the liquid used. Also, due to time constraints, the material should preferably be readily available.

An example of soft magnetic materials, which are materials with a high saturation and low coercivity, is shown in Figure 2.5. The permeability and cost can be seen for several groups of materials.
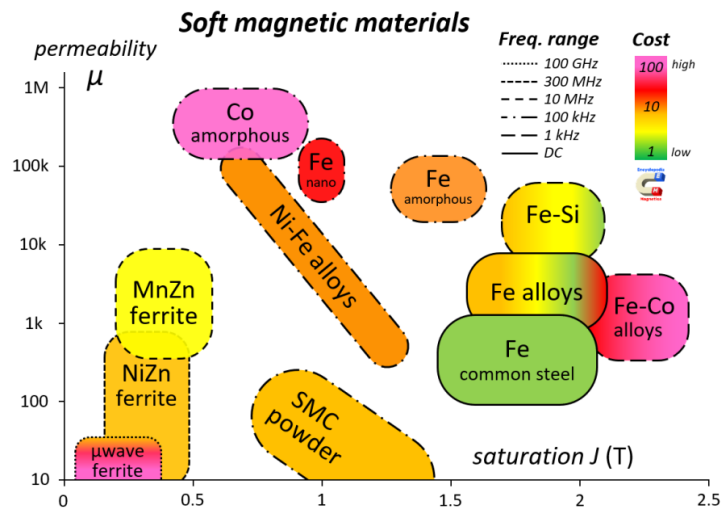
Figure 2.5: The permeability of soft magnetic materials with costs. This figure is reprinted/reused by permission from ©Iowa State University Center for Nondestructive Evaluation (CNDE) [8]. Licensed under CC BY-NC 4.0 International.

3 BREAKUP CALCULATIONS

Using the Rayleigh Plateau Instability the theoretical frequencies at which the jet breaks up can be calculated. The actual frequency can deviate from the theory due to the frequency response from the vibrating element or eigenfrequencies from the structural elements.

First of all, the Weber number, We, can be seen as the ratio of the inertial forces over the surface tension.

$$We = \frac{\rho U^2 2R}{\sigma} \tag{3.1}$$

with ρ [kg m^{-3}] as the density, U [m s^{-1}] the jet velocity of the alginate, R [m] the diameter of the nozzle and σ [N m^{-1}] the surface tension. By setting We the flow rate Q [m^3 s^{-1}] can be calculated. This is done to stay in the jetting regime. Alternatively, the jet velocity can be set as constant.

$$Q = \sqrt{\frac{\pi^2 R^3 We\sigma}{2\rho}} \tag{3.2}$$

Once these are known the Reynolds number is calculated.

$$Re = \frac{2\rho Q}{\pi \mu R} \tag{3.3}$$

With μ [Pa s] as the dynamic viscosity. Consequently, the Ohnesorge number, Oh, is calculated as well. If Oh is too large, the jet will be too viscous for breakup.

$$Oh = \frac{\sqrt{We}}{Re} \tag{3.4}$$

For determining the frequency at which the piezo or speaker should be vibrated, a dispersion relation for inviscid flows proposed by Rayleigh is used [9]:

$$\omega^2 = \frac{\sigma}{\rho R_0^3} kR_0 \frac{I_1(kR_0)}{I_0(kR_0)} \left(1 - k^2 R_0^2\right) \tag{3.5}$$

At kR_0 = 0.697 the most amplified wavelength is found, thus at the corresponding frequency pertubations grow the fastest. Filling this in results in the frequency in rad s^{-1}.

$$\omega^2 \approx \frac{\sigma}{\rho R_0^3} 0.1332 \tag{3.6}$$

To calculate the n'th eigenfrequency in Hz the following equation can be used. In practice this can be used as a guidance, although it sometimes is uncertain what the influence of factors like powder addition is. Therefore it is recommended to cycle over a range of a frequencies and select the best performing.

$$f_n = \frac{\omega_n}{2\pi} n \tag{3.7}$$

The We impact number also needs to be taken into account. In the supplementary material of [10] it was observed that for 1 < α < 1.3, there is almost no droplet deformation. With α defined as follows:

$$\alpha = \frac{U_{CaCl}}{U} \tag{3.8}$$

with U_{CaCl} [m s^{-1}] as the jet velocity of the calciumchloride jet.

7

4   PROOF OF CONCEPT

This chapter describes the setup and method used for the first experiments, of which the results are not included in the paper. The setup was later improved and those results are used in the paper.

4.1   Setup

4.1.1   Materials

The materials needed for the setup itself are as follows:

- 2 ProSense syringe pumps

- Fisherbrand™ 60 ml syringe (14955455) with 29.2 mm ID

- Fisherbrand™ 60 ml screw syringe (14955461) with 29.2 mm ID

- PK44M3B8P2 - Discrete Piezo Ring Stack, 150 V, 15 µm Displacement, 15.0 mm OD, 9.0 mm ID, 13.5 mm Long, Two Flat End Plates

- XIMEA camera (MC031MG-SY)

- BENECREAT blunt dispersing tip needle, 21 gauge. 0.52 mm ID, 0.81 mm OD

- Falco Systems WMA-100A high voltage amplifier. 20X amplification from −170 V to 170 V.

- RS PRO AFG21005 Function Generator, 0.1Hz Min, 5MHz Max, Variable Sweep

The chemicals which are needed are as follows:

- Sodium alginate 80-120

- Ethanol

- Neodymium powder, 25 µm

- Permalloy powder, 45 µm max

4.2   Method

First of all, prepare all the corresponding suspensions and solutions needed.

1. Prepare 200 g alginate solution with 0.5% Sodium alginate weight/weight, added with demi water.

2. Prepare a 60 mL CaCl (calcium chloride) solution, with $0.2 \, \text{mol} \, \text{L}^{-1}$ CaCl, 10% ethanol volume/volume, added with demi water.

3. Prepare 30 g suspensions of alginate with powder such that the weight/weight percentages of powder/ alginate solution is 0.5%, 5% and 10%.

4. Let the suspensions sit in a ultrasonic bath for thirty minutes.

While the suspensions are in the ultrasonic bath, prepare the setup.

1. Calculate the corresponding variables following from the Weber number and the Rayleigh Plateau instability, as described in chapter 3.

2. Set up the pumps with the right ID. Use the calculated flow rate for the alginate pump.

3. Enable the LED backlight and camera.

4. Load the corresponding syringes with the alginate solution without any added powder and the CaCl solution.

5. Test the camera setup with only alginate, such that the focus and backlight are suitable.

6. Test the CaCl jet, such that it reaches the alginate droplets as a jet, while still having a low impact angle.

7. Enable the amplifier and the function generator, select a sine wave.

8. Test whether the piezo works and if the alginate jet creates monodisperse droplets. Vary the frequency to test do this.

The setup should now be ready to use. It is useful to test it with a control sample of alginate solution without any powder. Besides, recording the process is recommended for inspecting the process. The steps to produce a sample are as follows.

1. Enable the amplifier and the function generator.

2. If using alginate with powder, shake the syringe before loading the pump.

3. Start the alginate pump first.

4. Check the monodispersity on the camera.

5. If ready, enable the CaCl pump. Make sure the petri dish is in reach.

6. Once a steady state is reached, hold the petri dish under the jets to catch the droplets.

7. Continue to do so till a sufficient sample size is reached.

8. Store the petri dish and disable all pumps.

4.3 Results

A selection of the samples is shown in Figure 4.1 for neodymium and Figure 4.2 for permalloy.
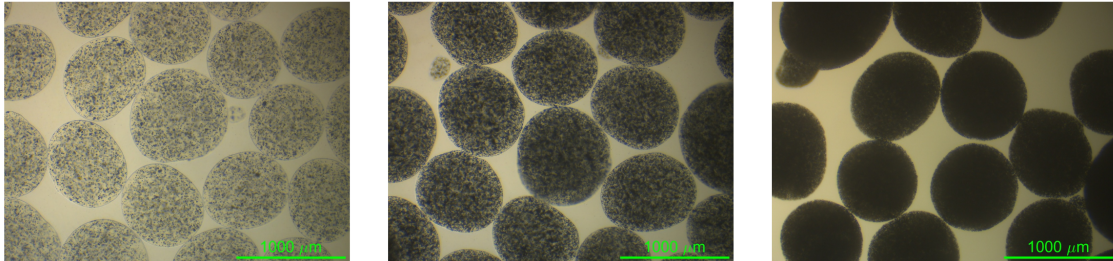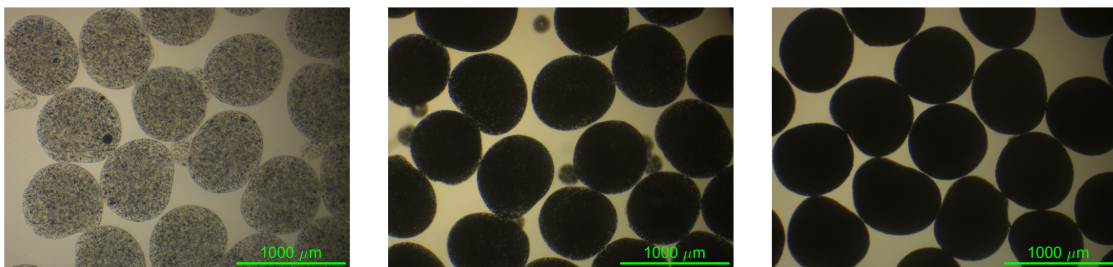
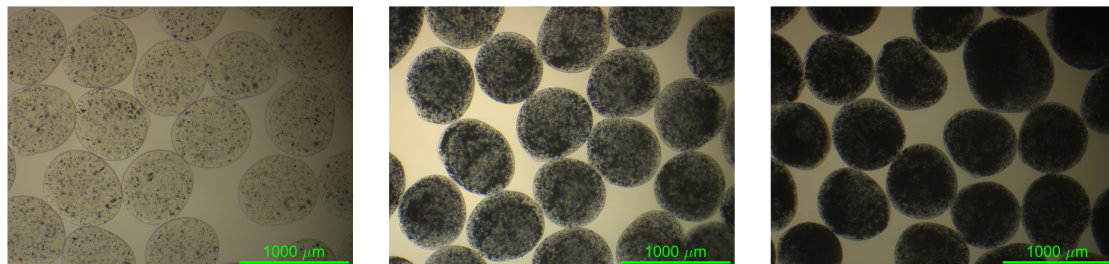Figure 4.1: Microscopic views of alginate beads with neodymium powder. From left to right, 0.5%, 5% and 10% wt/wt powder.
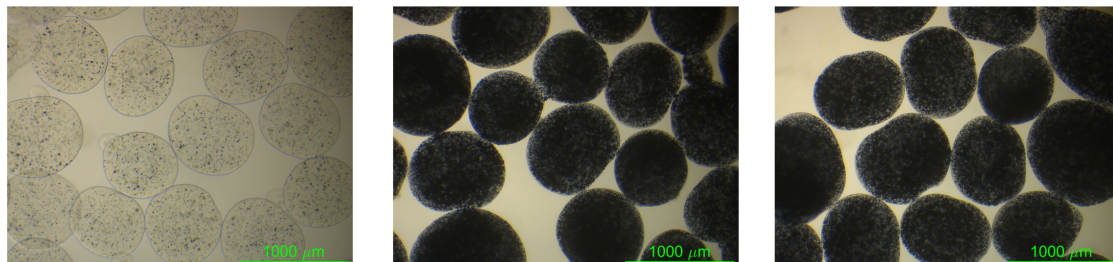
Figure 4.2: Microscopic views of alginate beads with permalloy powder. From left to right, 0.5%, 5% and 10% wt/wt powder.

5 IMPROVED SETUP

5.1 Setup

The setup used for the exixperiment can be seen in Figure 5.1.
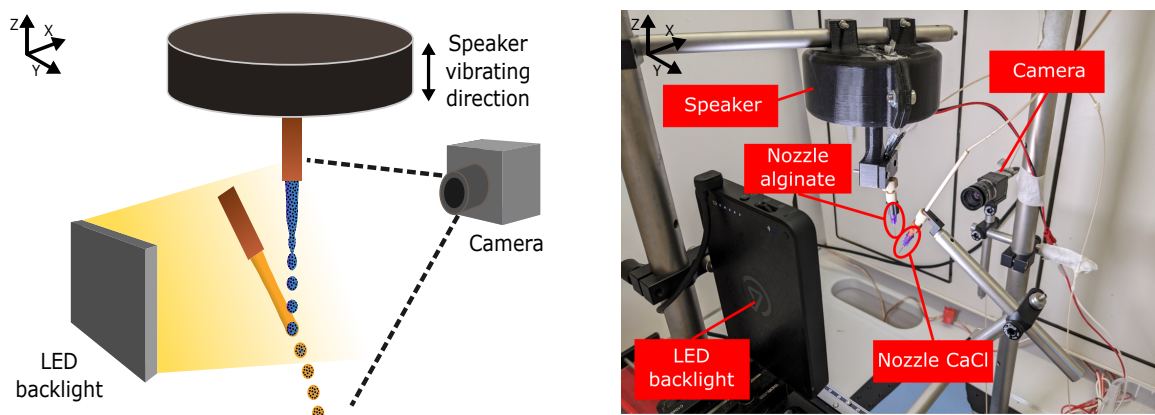
Figure 5.1: The setup used to create magnetic alginate beads.
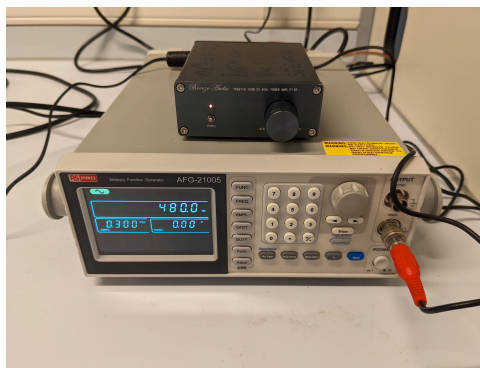
Figure 5.2: The function generator together with the amplifier used.

5.1.1 Materials

The materials needed for the setup itself are as follows:

- 2 ProSense syringe pumps

- 30 ml luer lock syringe with 22.6 mm ID

- Woofer
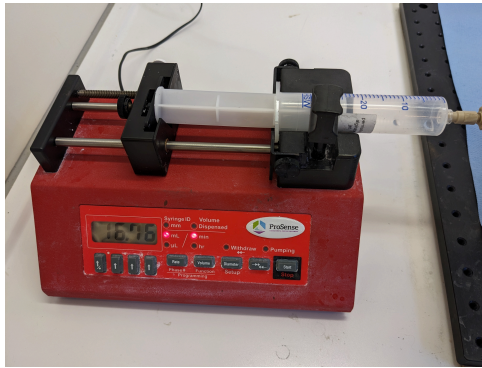
Figure 5.3: One of the pumps which was used in the setup.
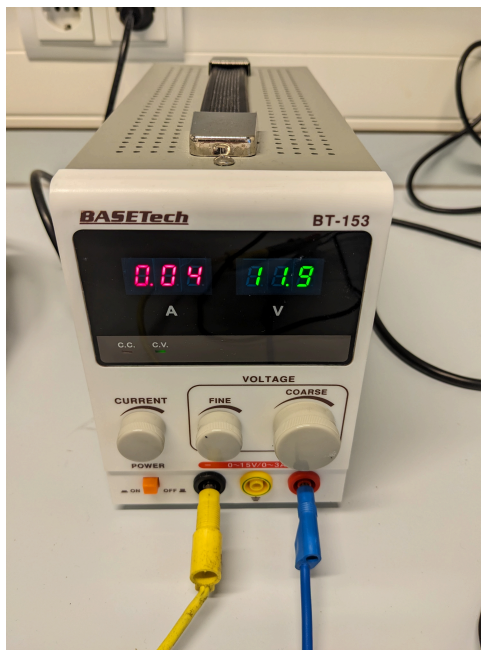
Figure 5.4: The power supply which was used.

- TPA3116D2 amplifier

- XIMEA camera (MC031MG-SY)

- LED backlight

- BENECREAT blunt dispersing tip needle, 21 gauge. 0.52 mm ID, 0.81 mm OD

- RS PRO AFG21005 Function Generator, 0.1Hz Min, 5MHz Max, Variable Sweep

- Basetech 12 V power supply

The chemicals which are needed are as follows:

- Sodium alginate 80-120

- Ethanol

- Neodymium powder, 25 µm

- Permalloy powder, 45 µm MAX

5.2 Method

The method does not differ from the previous setup and can be found in section 4.2.

5.3 Data acquisition and post-processing

The samples which were acquired were photographed using a Leica DM 300. These were used for a close up inspection of the particle properties like powder distribution and shape.

5.4 Results

5.4.1 Microscopy

Figure 5.5: Microscopic views of alginate beads with neodymium powder. From left to right, 0.5%, 5% and 10% wt/wt powder.

Figure 5.6: Microscopic views of alginate beads with permalloy powder. From left to right, 0.5%, 5% and 10% wt/wt powder.

6 SEM IMAGES OF POWDERS

The SEM images of the powders were taken with the NeoScope JCM-5000 as shown in Figure 6.1. The powders were put on the disk with double-sided tape and then loaded into the machine.

Figure 6.1: The NeoScope JCM-5000 used for taking the SEM pictures of the powders.

7 VSM

The powders were analysed in a PPMS® DynaCool™ Vibrating Sample Magnetometer (VSM) shown in Figure 7.1. To prepare the sample the powders were loaded in gelatine capsules and fixed with glue. The result is shown in Figure 7.2. As any movement of the powder can cause errors in the measurement, multiple samples were made to try. After producing the capsules, they were put in the tube of the VSM with a string to keep them in place.
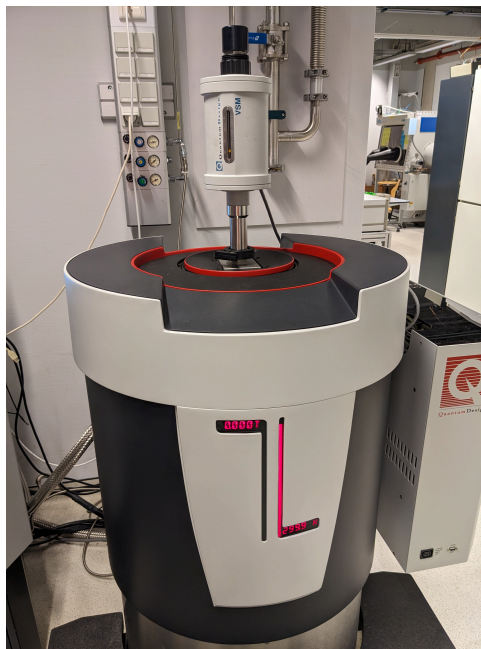
Figure 7.1: PPMS® DynaCool™ Vibrating Sample Magnetometer in the lab.

(a) All capsules, with neodymium on the left and permalloy on the right.

(b) Zoom of a permalloy capsule.

Figure 7.2: Gelatine capsules used for the VSM.

8 SIZE DISTRIBUTIONS

The particles were photographed and post-processed in MATLAB and Python to determine the size distributions. The photographing, post-processing and results are described here.

8.1 Photos

A Nikon D610 Camera and a macro lens with 60 mm focal length was put on a tripod. Every sample was put on an LED backlight under the camera. The scale was determined via the size of the LED backlight. In Figure 8.2 an example can be seen of a raw picture taken with the camera of a 5% permalloy sample. The high resolution allows for a proper post-processing. It is recommended to put effort into this as this will save time in the long run and increase the amount of particles which can be used in the post-processing.

For the control alginate particles without any powder the particles are less distinctive due to their transparency. Therefore it was also chosen to take a picture without any LED backlight. Instead a light was added next to the camera, together with a yellow background.
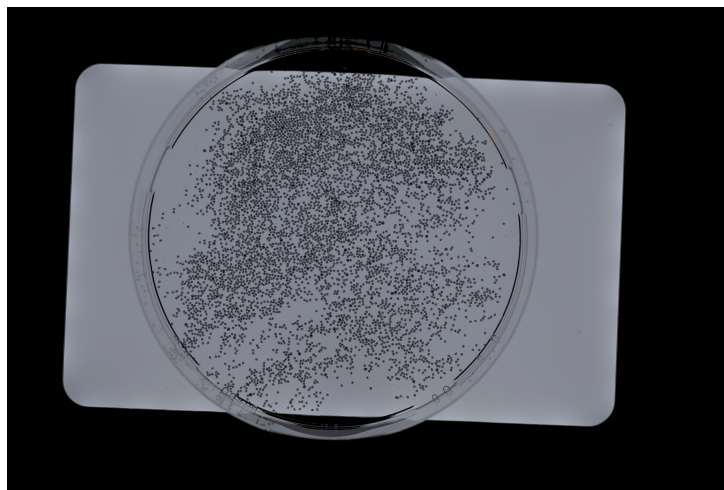
Figure 8.1: Raw picture of a 5% permalloy sample with an original resolution of 4028 by 6030.

8.2 Post-processing

The particle diameters were measured using the Hough transform. In MATLAB this is available with the command imfindcircles. Python also has an extensive library, called OpenCV, which allows for more precise tweaking. The particles with powder were processed in MATLAB, yet this did not work well for the control alginate particles. Therefore it was chosen to process these in Python as this offered more precise tuning of the Hough transform.

To optimise the detection of the particles, the images of the particles with powder are binarised and the alginate control particles are converted to grayscale and a CLAHE equalisation is ap-
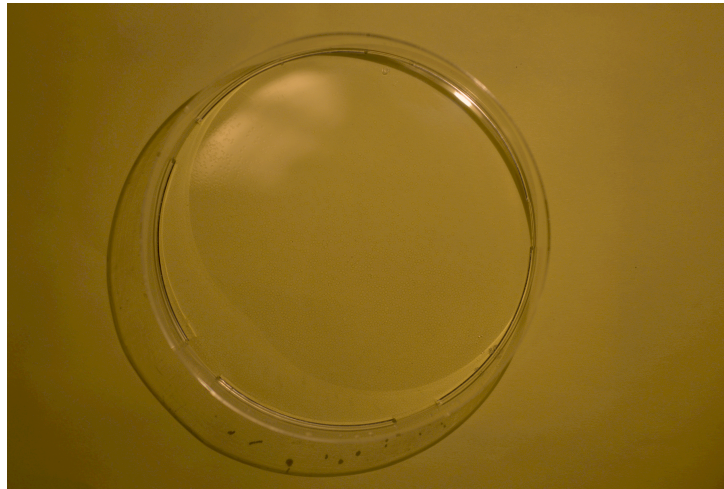
Figure 8.2: Raw picture of a plain alginate sample with an original resolution of 4028 by 6030.
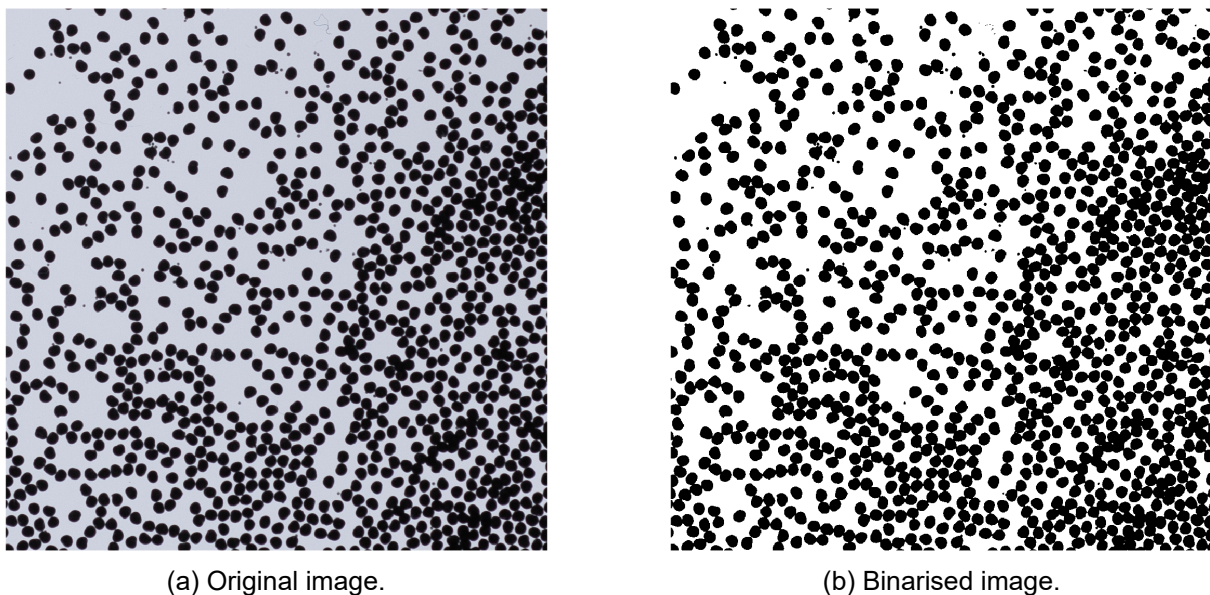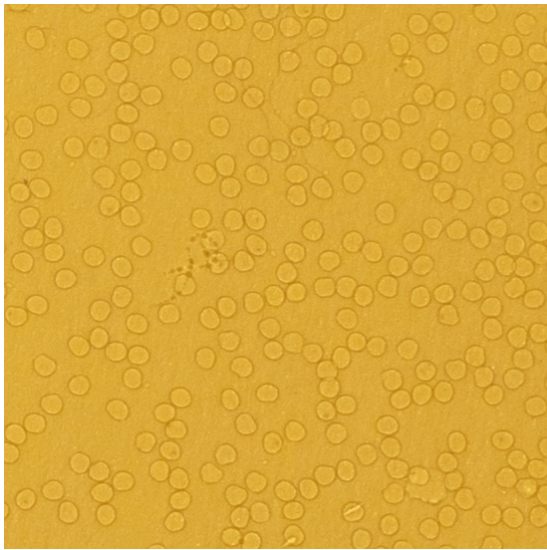

(a) Original image.

(b) Binarised image.

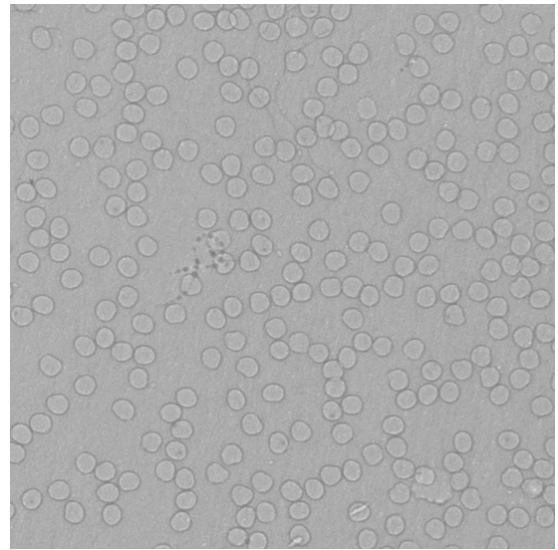Figure 8.3: Post-processing of alginate particles with 5% neodymium powder.

plied, as shown in Figure 8.3 and Figure 8.4 respectively, such that the borders of the particles are more apparent for the algorithm. A selection of a clear part of the picture is taken and Hough transform is applied to this. Particles close to the borders are removed due to the possibility of selecting particles which overlap with the border.

An example of the result of a Hough transform can be seen in Figure 8.5a. A zoom of the same figure is shown in Figure 8.5b. Small satellite particles were not taken into account by selecting a size range for the algorithm. It can be seen that the particles are not perfectly round.

The result of the alginate control sample is shown in Figure 8.6. As can be seen the particles are harder for the algorithm to detect. Instead of binarising this image it was chosen to apply a CLAHE to improve the contrast, as there is no powder in the particles. The challenging part here is to include the border of the alginate particle, requiring the testing of various input options of the algorithm.

(a) Original image.

(b) Grayscale and CLAHE applied.

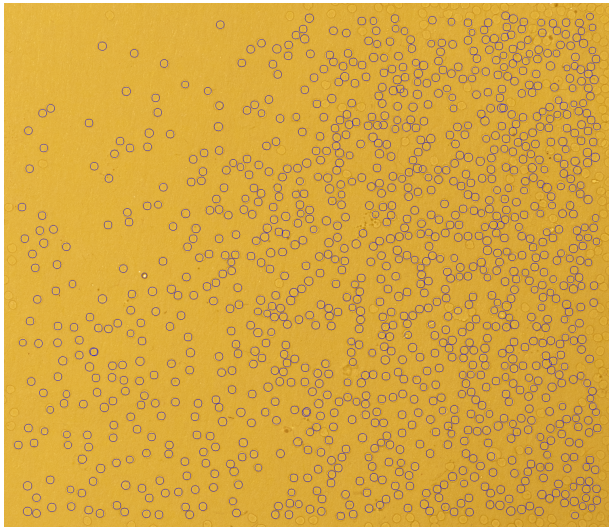Figure 8.4: Post-processing of control alginate particles.
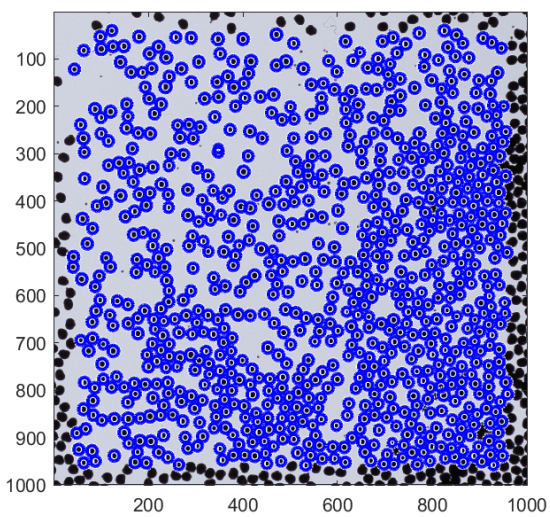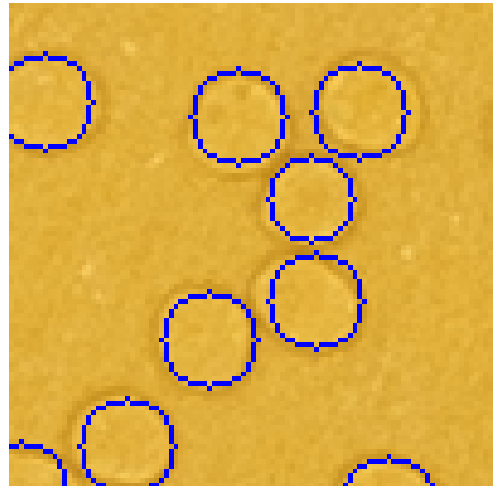

(a) The entire region taken into account.
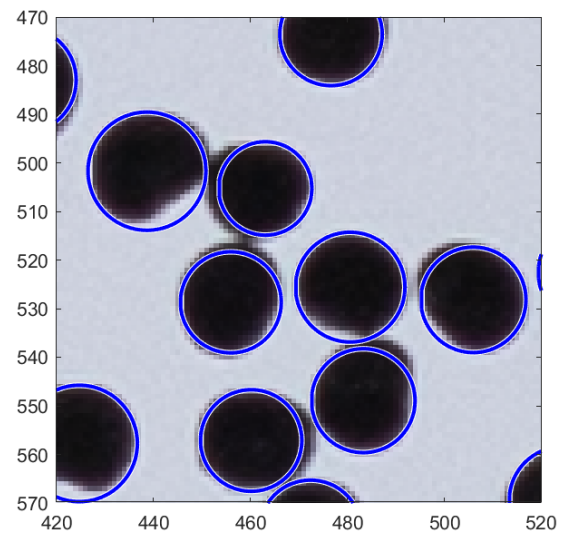
(b) A zoom of the left figure.

Figure 8.5: Results of the Hough transform for alginate particles with powder. Each circle is a spherical particle detected.

(a) The entire region taken into account.

(b) A zoom of the left figure.

Figure 8.6: Results of the Hough transform for alginate control particles without any powder. Each circle is a spherical particle detected.

8.3   Results

The results of the Hough transform can be seen in Figure 8.7a where every histogram represents a sample. These are made up of 580-987 particles, depending on the specific sample. The distribution of the alginate control particles with 1125 counted can be seen in Figure 8.7b.
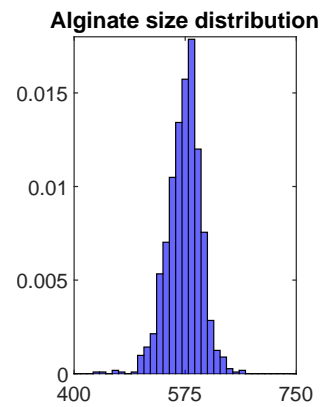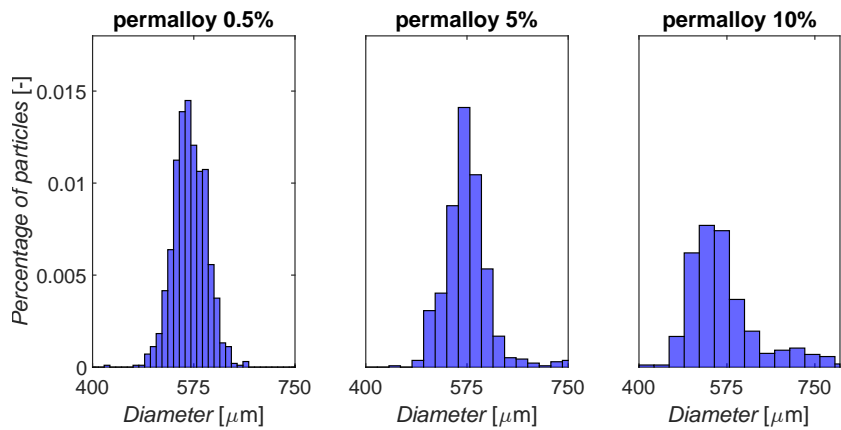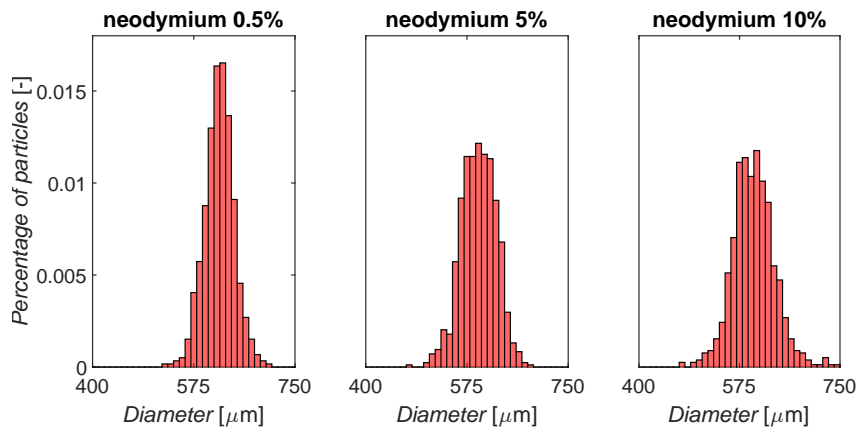
(a) Histograms of the size distributions of the neodymium (red) and permalloy (blue) particles. Bins are capped at 400 and 800.

(b) Histogram of the size distribution of the alginate control particles without powder.

9   CHARACTERISATION

9.1   Measurement of magnetic field

Measurement of the magnetic field was done using a Teslameter FM 302 with an AS-NTM transverse probe as seen in Figure 9.1a. The transverse probe was moved with a 1D stage as shown in Figure 9.1b.
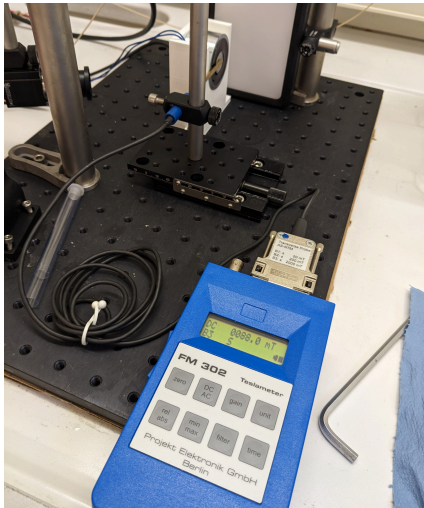
(a) The Teslameter used for measuring the magnetic field strength.
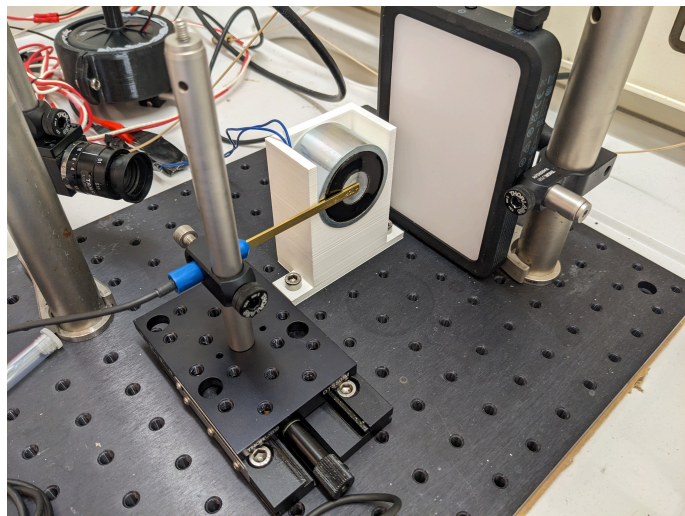
(b) The transverse probe on the 1D stage in the setup.

The results of the magnetic field measurements are shown in Figure 9.2. An exponential equation was applied for usage in the trajectory solver with a and b as fitting parameters, which were optimised by a least squares algorithm.

$$H = ae^{xb} \tag{9.1}$$

9.2   Prediction of trajectory

To be able to predict the trajectory of the particle, the resolution of the video was calibrated by the diameter of the pillar. Following this, the diameter of the particle was measured in the video. Once the particle started moving, its movement was tracked. The starting position is defined as the last position where the y difference between that frame and the start is smaller than 50 μm. This is done to make sure to eliminate starting conditions which are not modelled in the theory, specifically the departure from the pillar. The end position is defined as the position where the particle stops moving, when it is stuck to the container, or when the circle is not detected for multiple frames.
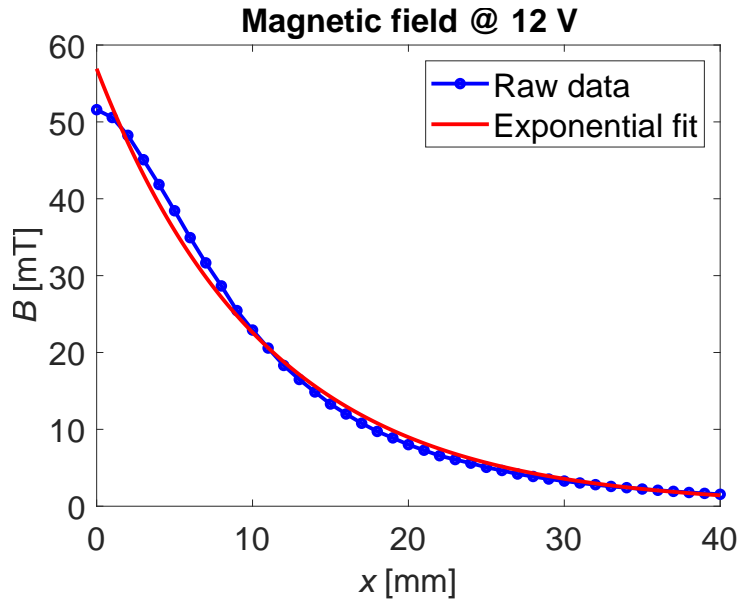
Figure 9.2: The magnetic field measured at 12 V together with a least square fit of an exponential function.

9.2.1   Calibrating drag

For calibrating the drag coefficient of the particles, particles were dropped into the container without any magnetic field. The particles fell significantly faster compared to the theoretical trajectory of a smooth sphere. Therefore it was decided to calibrate the drag coefficient using the existing equation and a factor α. Alginate densities are typically slightly higher than water [11], yet it is challenging to determine the exact density of a particle. From the experiments it followed that an alginate density of $1015 \, \mathrm{kg \, m^{-3}}$ and $\alpha = 0.18$ had the best fit. The results are shown in Figure 9.4a.

9.3   Measurement of trajectory

The measurement of the trajectory of the particles under influence of the magnetic field was done with the setup in Figure 9.5. A pillar was designed with a 2.2 mm diameter at the top, on which the particles can be placed. To add ballast, two non-magnetic 10 cent coins were inserted at the bottom.

In the experiment, a particle is placed on the pillar, which is positioned on the line perpendicular to the centre of the magnet. Then the camera, a XIMEA camera (MC031MG-SY), starts recording. The magnet is switched on and the the particle either starts moving or stays at its place. When the particle stays at its place, the magnetic force is not high enough and the pillar needs to be moved closer to the magnet.
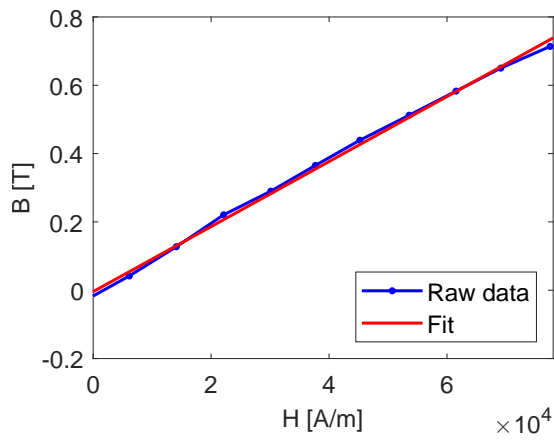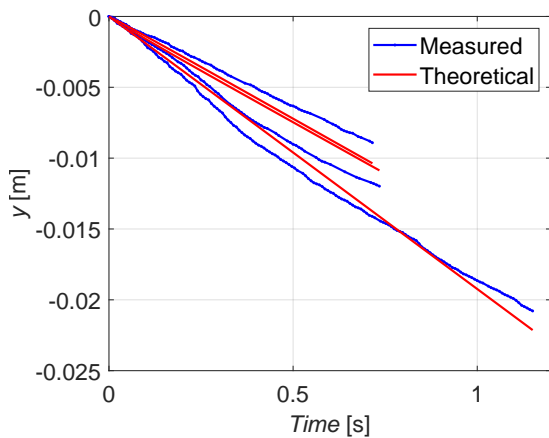
(a) The hysteresis loop of permalloy fitted with a first order polynomial.
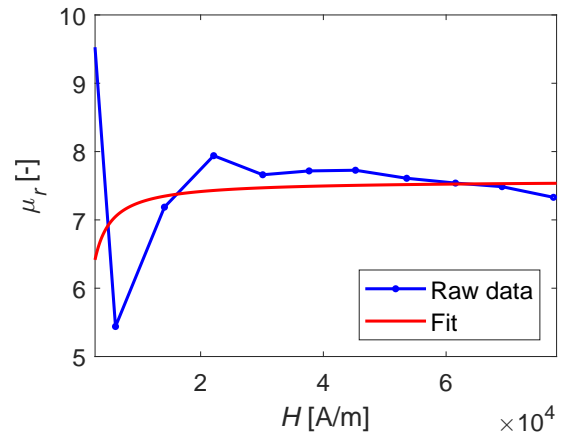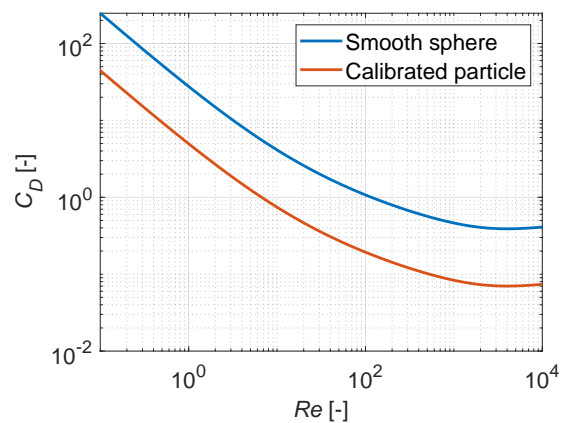

(b) The relative permeability of permalloy together with the first order polynomial fit.

Figure 9.3: Fitting of the hysteresis loop of permalloy to get a fit of the relative permeability. Valid from about $2.8\,\mathrm{kA\,m^{-1}}$ to $78\,\mathrm{kA\,m^{-1}}$ or $3.52\,\mathrm{mT}$ to $98.02\,\mathrm{mT}$.
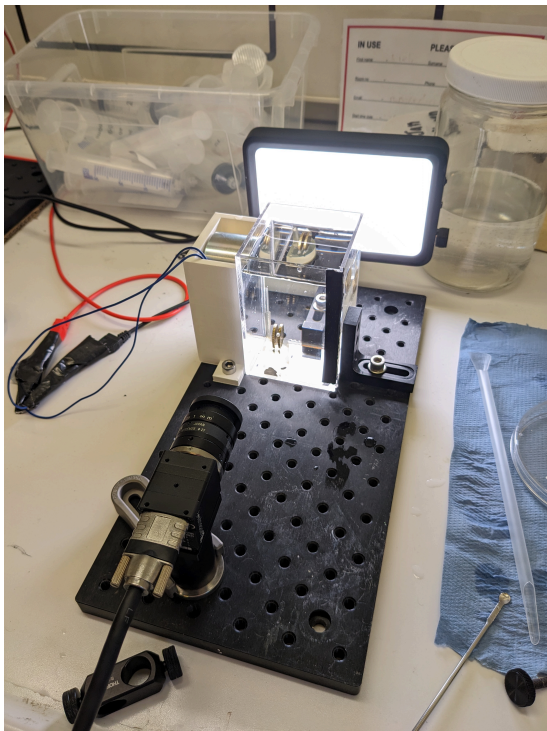

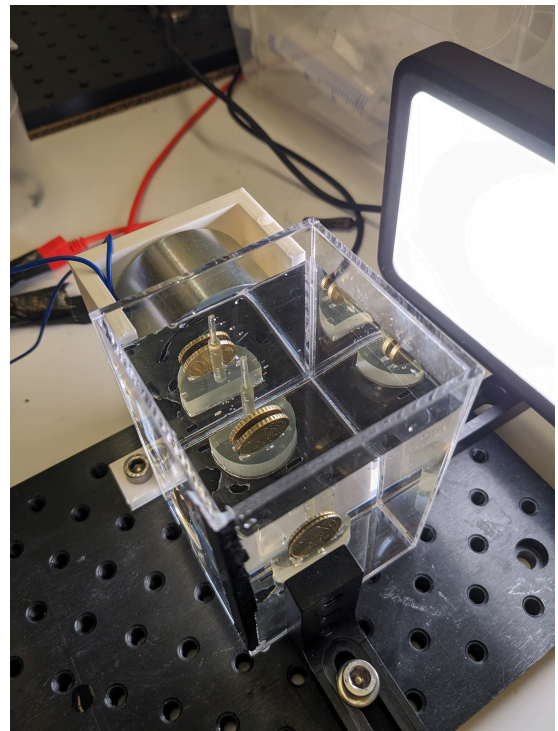(a) Measured trajectories of falling particles and the fitted trajectory.

(b) Comparison of the drag coefficient with a smooth sphere.

Figure 9.4: The measurement and calibration of the drag of alginate particles made with 0.5% permalloy powder.

(a) Side view.

(b) Top view.

Figure 9.5: The setup to measure the particle trajectories.

REFERENCES

[1] J. M. D. Coey, *Magnetism and Magnetic Materials*, 1st ed. Cambridge: Cambridge University Press, 2010. ISBN 978-0-511-67743-4. [Online]. Available: www.cambridge.org/9780521816144

[2] "Wikipedia," accessed on 04-12-2023. [Online]. Available: https://en.wikipedia.org/wiki/File:VFPt_cylindrical_magnet_thumb.svg

[3] R. Nisticò, F. Cesano, and F. Garello, "Magnetic Materials and Systems: Domain Structure Visualization and Other Characterization Techniques for the Application in the Materials Science and Biomedicine," *Inorganics 2020, Vol. 8, Page 6*, vol. 8, no. 1, p. 6, jan 2020. doi:10.3390/INORGANICS8010006.

[4] J. Svoboda, *Magnetic Techniques for the Treatment of Materials*, 1st ed. Dordrecht: Kluwer Academic Publishers, 2004. ISBN 1402021070. [Online]. Available: http://www.ebooks.kluweronline.com

[5] "Nondestructive Evaluation Physics : Magnetism," accessed on 19-09-2023. [Online]. Available: https://www.nde-ed.org/Physics/Magnetism/electricmotor.xhtml

[6] "Magnetic Permeability — Electromagnetic Geophysics," 2018, accessed on 26-09-2023. [Online]. Available: https://em.geosci.xyz/content/physical_properties/magnetic_permeability/index.html

[7] Netzsch, "Curie Temperature - NETZSCH Analyzing & Testing," accessed on 20-10-2023. [Online]. Available: https://analyzing-testing.netzsch.com/en/training-know-how/glossary/curie-temperature

[8] "Nondestructive Evaluation Physics : Magnetism," accessed on 16-10-2023. [Online]. Available: https://www.nde-ed.org/Physics/Magnetism/index.xhtml

[9] J. Eggers and E. Villermaux, "Physics of liquid jets," *Reports on Progress in Physics*, vol. 71, no. 3, p. 036601, feb 2008. doi:10.1088/0034-4885/71/3/036601.

[10] C. W. Visser, T. Kamperman, L. P. Karbaat, D. Lohse, and M. Karperien, "In-air microfluidics enables rapid fabrication of emulsions, suspensions, and 3D modular (bio)materials," *Science Advances*, vol. 4, no. 1, jan 2018. doi:10.1126/sciadv.aao1175.

[11] P. Del Gaudio, P. Colombo, G. Colombo, P. Russo, and F. Sonvico, "Mechanisms of formation and disintegration of alginate beads obtained by prilling," *International Journal of Pharmaceutics*, vol. 302, no. 1-2, pp. 1–9, sep 2005. doi:10.1016/J.IJPHARM.2005.05.041.